

# A humidity-entrainment mechanism for microphysical invigoration of convection

Tristan H. Abbott<sup>a</sup> and Timothy W. Cronin<sup>a</sup>

<sup>a</sup>Department of Earth, Atmospheric and Planetary Sciences, Massachusetts Institute of Technology, Cambridge, MA 02139

This manuscript was compiled on February 17, 2020

Cloud-aerosol interactions are thought to influence vertical velocities in deep convection, and past research has proposed several mechanisms which which high aerosol concentrations might invigorate convection. However, these mechanisms largely ignore coupling between clouds and their environment and therefore neglect possible invigoration mechanisms that involve that coupling. In this work, we propose a novel invigoration mechanism that arises through the influence of aerosols on environmental humidity. We find that increasing the liquid cloud droplet number concentration ( $N_c$ , a proxy for aerosol concentration) produces robust increases in peak vertical velocities in idealized convection-permitting simulations. We show that environmental humidity also increases robustly with  $N_c$ , and we use calculations with simple entraining plume models to link the humidity increase to warmer and faster updrafts. Additionally, we argue that humidity increases at high  $N_c$  because clouds form rain less readily and instead detrain more condensate into their environment. Finally, we show that links between aerosol concentration and peak vertical velocity are weakened in scenarios where strong large-scale forcing replaces cloud detrainment as the dominant control on atmospheric humidity. Our results emphasize the importance of interactions between clouds and their environment in determining the cloud-scale response to changes in cloud microphysics and suggest that a possible response to increased aerosol loading is invigoration by a "humidity-entrainment" mechanism.

cloud dynamics | aerosols | tropical weather and climate

Observations suggest cloud-aerosol interactions may play a significant role in setting vertical velocities in deep convective clouds. Direct measurements of updraft velocities themselves are scarce, but many studies have found increases in cloud top height and cloud cover coincident with increases in aerosol loading (e.g. 1–6). Additionally, lightning flash rates are consistently higher in regions of the tropics with high aerosol abundance, including continents, islands, and ship tracks (e.g. 7–10). Together, these observations suggest that high aerosol concentrations may trigger a chain of processes that ultimately leads to an increase in the strength of convective updrafts—which we refer to throughout this paper as “microphysical invigoration”. Understanding whether and how microphysical invigoration arises enhances our understanding of severe weather risks associated with thunderstorms and of climatically-important cloud properties (e.g. 11–14), and is particularly relevant today because human activity is a major aerosol source.

Past work has proposed two mechanisms by which aerosol concentrations could affect vertical velocities. The first mechanism relies on a “cold-phase” pathway: higher concentrations of cloud condensation nuclei (particles that provide surfaces on which liquid cloud droplets condense) suppress rain in shallow clouds, allowing clouds to loft more condensate through the freezing level and increasing the latent heat released when

cloud water freezes (15). The second mechanism relies on a “warm-phase” pathway: higher aerosol concentrations reduce supersaturation in liquid clouds, increasing latent heat release through additional condensation of water vapor (16).

Both of these mechanisms are founded on an undilute-parcel view of convective clouds, but real clouds are tightly coupled to their environments. Thus, microphysical invigoration may encompass not only the impact of aerosols on cloud processes, but also feedbacks that arise from the influence of cloud processes on the environment. Cloud processes have a first-order effect on mean tropical relative humidity through the detrainment of moist air (17, 18), and recent work shows that microphysical perturbations can alter environmental humidity by modifying re-evaporative moistening (19). In turn, environmental humidity mediates updraft buoyancy through entrainment (20). Here, we use idealized high-resolution model simulations to demonstrate a clear link between cloud microphysics and peak vertical velocities, and moreover to show that this link arises through a novel “humidity-entrainment” mechanism that relies specifically on the interaction between clouds and their environment.

## Invigoration with parameterized large-scale dynamics

We represent changes in aerosol abundance in our simulations by varying a prescribed liquid cloud droplet number concentration ( $N_c$ ) in the model’s cloud microphysics scheme (21) from  $50 \text{ cm}^{-3}$  (characteristic of pristine maritime environments) to  $800 \text{ cm}^{-3}$  (characteristic of very polluted continental environments) (22). Because larger  $N_c$  inhibits rain formation

### Significance Statement

Observations show that tropical thunderstorms are often stronger when concentrations of aerosol particles in the atmosphere are higher. However, the physical processes that link aerosols to thunderstorm strength are complex, multi-scale, and poorly understood. In this paper, we use high-resolution atmospheric simulations to show that high aerosol concentrations can produce thunderstorms with stronger updrafts by increasing the humidity of the surrounding atmosphere. Our work provides a novel hypothesis for the causal link between aerosols and thunderstorm intensity, suggests a target for future observational analysis, and has implications for understanding how man-made aerosols alter the weather and climate of Earth’s tropics.

T.H.A. and T.W.C. designed research; T.H.A performed research and analyzed data; and T.H.A and T.W.C. wrote the paper.

The authors declare no conflicts of interest.

<sup>2</sup>To whom correspondence should be addressed. E-mail: thabbott@mit.edu

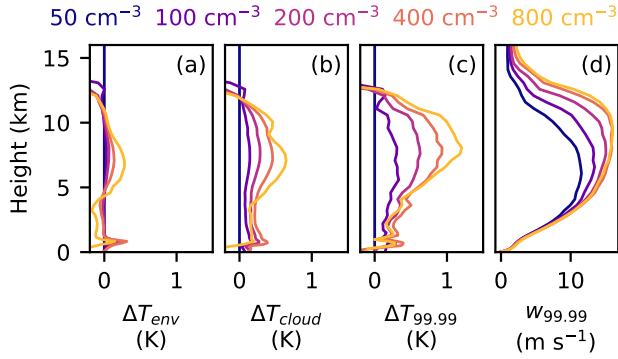


**Fig. 1.** Temperature and vertical velocity profiles in WTG simulations. Panels (a-c) show differences from a control WTG simulation (with  $N_c = 50 \text{ cm}^{-3}$ ) in (a) domain- and time-mean temperatures ( $T_{\text{env}}$ ), (b) mean temperatures in cloudy updrafts ( $T_{\text{cloud}}$ ), and (c) 99.99th percentile temperatures at each level ( $T_{99.99}$ ). Panel (d) shows 99.99th percentile vertical velocities at each level. Cloudy updrafts in (b) are defined as grid points with vertical velocities above  $1 \text{ m s}^{-1}$  and cloud water mixing ratios above the smaller of  $10^{-2} \text{ g kg}^{-1}$  or 1 percent of the saturation specific humidity.

in liquid clouds (23), the cold-phase invigoration mechanism could plausibly enhance updraft speeds in simulations with higher  $N_c$ . However, we configure the microphysics scheme to allow no supersaturation in liquid clouds, precluding the operation of the warm-phase invigoration mechanism.

We first consider simulations that include a parameterization of large-scale dynamics based on the weak temperature gradient (WTG) approximation (24, and see *Materials and Methods*). The WTG parameterization requires a reference temperature profile as input and diagnoses large-scale vertical motion that both relaxes domain-average temperature profiles toward the reference profile and generates large-scale moisture convergence. We configure WTG-constrained simulations to mimic a localized aerosol anomaly embedded within a large-scale low aerosol environment, but with otherwise identical boundary conditions, by taking the reference temperature profile from an  $N_c = 50 \text{ cm}^{-3}$  simulation of radiative-convective equilibrium (RCE), where the environment evolves freely until reaching an equilibrium where heating by convection balances cooling by radiation.

Increasing  $N_c$  increases peak vertical velocities in WTG simulations by up to 100% in the upper troposphere. Because of the constraints imposed by WTG dynamics, environmental temperature profiles vary little with  $N_c$  (Figure 1a). However, increasing  $N_c$  results in warmer temperatures in cloudy updrafts (Figure 1b) as well as increases in the warmest temperatures at each level (Figure 1c). Warmer updrafts in high- $N_c$  simulations attain higher buoyancies, and peak vertical velocities increase with increasing  $N_c$  as a result (Figure 1d). This result—invigoration in simulations with a localized aerosol anomaly—is consistent with results from other modeling studies, although past work has represented aerosol anomalies using spatially inhomogeneous RCE simulations (25, 26) rather than by parameterizing large-scale dynamics.

As previous studies (25, 26) have noted, circulations that link low- and high-aerosol regions are critical for allowing aerosol increases to invigorate convection. If we remove the WTG parameterization (which represents such circulations) and instead run RCE simulations with varied  $N_c$  (*Materials*

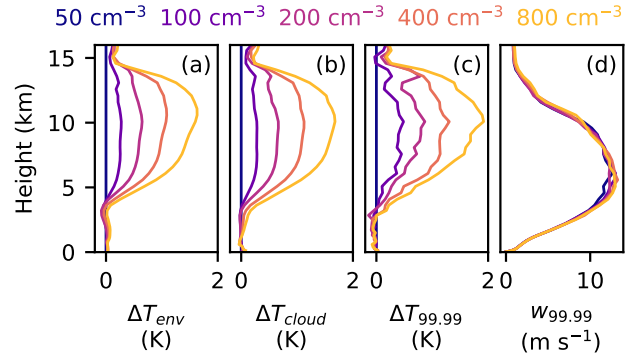


**Fig. 2.** Temperature and vertical velocity profiles in RCE simulations. Panels (a-c) show differences from a control RCE simulation (with  $N_c = 50 \text{ cm}^{-3}$ ) in (a) domain- and time-mean temperatures ( $T_{\text{env}}$ ), (b) mean temperatures in cloudy updrafts ( $T_{\text{cloud}}$ ), and (c) 99.99th percentile temperatures at each level ( $T_{99.99}$ ). Panel (d) shows 99.99th percentile vertical velocities at each level.

and *Methods*), increasing  $N_c$  no longer strengthens intenset updrafts. Instead, gravity waves cause environmental temperatures (Figure 2a) to warm by almost exactly the same amount as temperatures in updrafts (Figures 2b,c), preventing warmer updrafts in high- $N_c$  simulations from attaining additional buoyancy. As a result, peak vertical velocities are nearly identical in all RCE simulations (Figure 2d). This finding that cloud buoyancies in RCE are little altered by  $N_c$  mirrors previous work (25, 27): global mechanisms that produce warmer updrafts do not generate more buoyant or faster updrafts.

### Humidity-entrainment invigoration mechanism

Despite the lack of invigoration in RCE simulations, they are a valuable tool for probing the mechanisms that produce invigoration in WTG simulations. Because increasing  $N_c$  increases updraft temperatures in both RCE and WTG simulations, understanding the processes that warm updrafts in RCE simulations should provide insight into invigoration in WTG simulations. Additionally, focusing on RCE simulations allows to us investigate causal links between changes in microphysics and updraft temperatures without the complexity introduced by the coupling between convection and large-scale circulations.

Because cold-phase invigoration mechanisms rely on the latent heat of fusion, we test whether they are responsible for the warmer troposphere in high- $N_c$  RCE simulations by conducting mechanism denial experiments with the latent heat of fusion  $L_f$  set to 0. We find that differences between low- and high- $N_c$  temperature profiles with  $L_f = 0$  are almost identical to the default simulations (Figure 3a); the persistence of the temperature differences provides strong evidence that the cold-phase mechanism is not responsible for warming the upper troposphere in high- $N_c$  simulations of RCE.

If not the latent heat of fusion, then what produces a warmer troposphere in simulations with higher  $N_c$ ? Humidity changes are one possibility: previous work has shown that updraft temperatures are closely linked, through entrainment, to environmental relative humidity (28). Moreover, scale analysis suggests that differences in relative humidity are likely to be a stronger control on updraft temperatures than differences in the mass of frozen condensate.

Using  $\Delta$  to denote differences between simulations with different microphysical properties, the impact of changes in the amount of frozen cloud condensate on parcel temperatures scales like

$$\Delta T_{\text{freeze}} = \frac{L_f}{c_p} \Delta q_{c,\text{freeze}}, \quad [1]$$

where  $\Delta T_{\text{freeze}}$  is the temperature change produced by an increase in the amount of frozen condensate of  $\Delta q_{c,\text{freeze}}$  and  $c_p$  is the heat capacity of air, respectively. Deep convective clouds have peak cloud water concentrations of around  $3 \text{ g kg}^{-1}$  (29, 30). This upper bound on  $\Delta q_{c,\text{freeze}}$  gives

$$\Delta T_{\text{freeze}} \lesssim 1 \text{ K}; \quad [2]$$

actual values of  $\Delta q_{c,\text{freeze}}$  and  $\Delta T_{\text{freeze}}$  are likely to be substantially smaller.

The impact of changes in environmental humidity on parcel temperatures—as felt through entrainment—scales like

$$\Delta T_{\text{entrain}} = \frac{L_v}{c_p} \epsilon \Delta RH \int_0^\infty q^*(z') dz', \quad [3]$$

where  $\Delta T_{\text{entrain}}$  is the temperature difference resulting from an environmental relative humidity difference  $\Delta RH$  (28, and see *Materials and Methods*).  $L_v$  is the latent heat of vaporization,  $\epsilon$  is an entrainment rate, and  $q^*$  is saturation specific humidity. Approximating  $q^*(z)$  as an exponential with a decay height of  $H_q = 2 \text{ km}$  allows us to re-write  $\Delta T_{\text{entrain}}$  as

$$\Delta T_{\text{entrain}} = \frac{L_v}{c_p} \epsilon H_q q_s^* \Delta RH. \quad [4]$$

If we use  $q_s^* \approx 20 \text{ g kg}^{-1}$  (corresponding to a surface temperature of about  $300 \text{ K}$ ) and an entrainment rate of  $1 \text{ km}^{-1}$  (typical for convective clouds, see e.g. 31), this gives

$$\Delta T_{\text{entrain}} \approx 100 \text{ K} \times \Delta RH. \quad [5]$$

This means that an increase in relative humidity of just 1 % can change parcel temperatures by  $\sim 1 \text{ K}$ , and more generally that parcel temperatures are likely to be much more sensitive to changes in environmental humidity than to changes in cloud water concentrations.

A simple plume model, which reproduces tropospheric warming in response to increasing humidity, provides additional evidence that changes in humidity are responsible for warming the troposphere in high- $N_c$  simulations (*Materials and Methods*). Mean specific humidity profiles in RCE simulations increase with  $N_c$  between 2.5 and 7.5 km (Figure 3b). Because plume temperatures are decreased less by entrainment in a moister environment, the plume model predicts warmer temperature profiles in high- $N_c$  simulations above about 3 to 4 km, approximately coincident with the level where simulated temperature differences first become large (Figure 3c). Choosing  $\epsilon = 1 \text{ km}^{-1}$  also approximately reproduces the magnitude of temperature differences in the upper troposphere, although this is sensitive to the choice of entrainment rate. A similar plume calculation can reproduce changes in high-percentile temperatures in WTG-constrained simulations given changes in mean humidity (see Supporting Information Text 1 and Figure S1 for details).

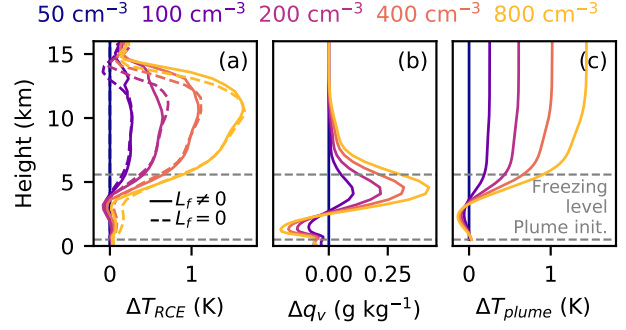


**Fig. 3.** Differences from an  $N_c = 50 \text{ cm}^{-3}$  control of (a) domain- and time-mean temperature profiles from RCE simulations with default  $L_f$  (solid lines) and  $L_f = 0$  (dashed lines), (b) Domain- and time-mean specific humidity profiles from RCE simulations used as input for plume calculations, and (c) environmental temperature profiles from plume calculations (details in text). The gray dashed line at 500 m shows the level where plume calculations are initialized with domain- and time-mean temperatures from simulations, and the gray dashed line near 5 km indicates the level where clouds begin to freeze, calculated as the lowest model level where more than 5% of the mean cloud water mass is ice. (Only one line is shown because this definition of the freezing level is identical in all simulations.)

### Why do aerosols produce a more humid environment?

Recently-developed analytic models for relative humidity in RCE (17, 18) provide a framework for understanding why the high- $N_c$  simulations have a moister atmosphere. By identifying relative humidity as the result of a balance between moistening by air detrained from clouds and drying by clear-air subsidence, these models provide expressions for RCE relative humidity of the form

$$RH \approx \frac{\delta_T}{\delta_T + \gamma}. \quad [6]$$

Here,  $\delta_T$  is a fractional detrainment rate per unit distance (dimensions of inverse length) that represents moistening by mixing saturated air and condensate from clouds into the environment, and  $\gamma = -\partial_z \ln q_e^*$  represents the inverse of the length scale over which subsidence dries the atmosphere.

By inhibiting the formation of rain in liquid clouds, increases in aerosol concentrations may increase the mass of condensate in air detrained below the freezing level, which in turn acts to increase tropospheric relative humidity by increasing  $\delta_T$  (18). Two features of the RCE simulations are consistent with aerosol-induced changes in detrainment moistening. First, clouds in high- $N_c$  simulations show larger condensate concentrations below the freezing level (Figure 4a); the higher moisture content of air detrained from such clouds would be consistent with increased detrainment moistening driving increased humidity. Second, a decrease in net precipitation source below the freezing level in high- $N_c$  simulations (Figure 4b) is consistent with aerosols increasing cloud water concentrations by inhibiting rain formation in liquid clouds. The smaller precipitation source could also be caused by increased precipitation evaporation, although this seems unlikely given the increased humidity in high- $N_c$  simulations.

### Sensitivity of invigoration to large-scale forcing

Analytic models for relative humidity make another prediction that can be used to test the detrainment-moistening link between aerosol concentrations and tropospheric humidity. If

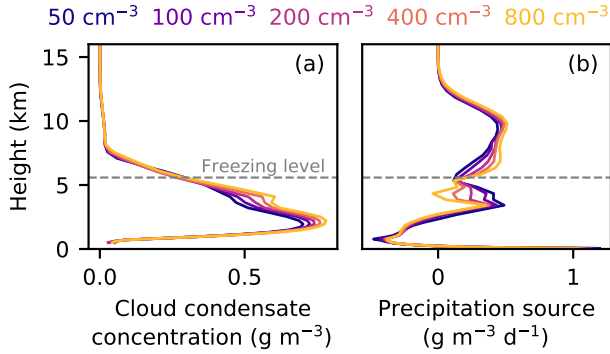


**Fig. 4.** (a) In-cloud condensate concentration and (b) net precipitation source profiles from RCE simulations. The in-cloud condensate concentration is calculated as a conditional average over all grid cells where the liquid plus ice cloud mass concentration is larger than then smaller of  $10^{-2}$   $\text{g kg}^{-1}$  and 1% of the saturation specific humidity. The net precipitation source, calculated as the vertical derivative of the precipitation flux profile, includes sources from cloud water and sinks from precipitation evaporation. The grey dashed line indicates the freezing level calculated as in Figure 3.

modified to include the effects of large-scale vertical motion, expressions for relative humidity become

$$RH = \frac{\delta_T}{\delta_T + \frac{M_d}{M_u} \gamma}, \quad [7]$$

where  $M_d$  is the downward clear-air mass flux and  $M_u$  is the in-cloud updraft mass flux (18). For reasonable values of  $\delta_T$ ,  $M_d/M_u$ , and  $\gamma$ , this implies that relative humidity becomes less sensitive to changes in detrainment moistening under the influence of large-scale upward motion (see Supporting Information Text 2 and Figure S2). If changes in  $N_c$  influence tropospheric humidity primarily by altering the detrainment of condensed water, this in turn implies that relative humidity should become less sensitive to  $N_c$  as large-scale ascent increases.

We test this prediction in two ways: first, by performing additional RCE simulations with an imposed large-scale vertical velocity profile given by

$$w = \begin{cases} w_0 \sin(\pi z/H) & z \leq H \\ 0 & z > H, \end{cases} \quad [8]$$

with  $H = 13$  km, similar to (18); and second, by using a set of WTG simulations where large-scale motion is induced by changing SST (*Materials and Methods*; Supporting Information Text 3 and Figure 3).

As  $w_0$  increases from 0 to 1 and then  $5 \text{ cm s}^{-1}$  in RCE simulations with imposed vertical motion, increases in  $N_c$  have a progressively smaller impact on relative humidity (Figure 5a). Similarly, inducing large-scale ascent by increasing SST in WTG simulations weakens the sensitivity of relative humidity (and peak updraft velocity) to  $N_c$  (Figure 5b,c), and sensitivity to  $N_c$  is largest in regimes with weak subsidence (small SST decreases). All these results are consistent with higher  $N_c$  promoting higher relative humidity by increasing detrainment moistening below the freezing level. The WTG simulations may also help to explain why a recent study (32) found only a weak link between aerosol concentrations and precipitation in a similar set of WTG-constrained simulations: that study focused primarily on convection strongly forced by a +2K SST perturbation.

## Conclusions

Previously-proposed invigoration pathways focused largely on processes that occur exclusively within clouds, including changes in the amount of condensate lofted through the freezing level (the “cold-phase” mechanism) and supersaturation in liquid clouds (the “warm-phase” mechanism). Our results, in contrast, emphasize the importance of interactions between clouds and their environment in determining the cloud-ensemble response to changes in cloud microphysics. The “humidity-entrainment” mechanism that is responsible for invigoration in our simulations is intrinsically linked to the role that convective clouds play in determining environmental humidity.

A contemporaneous modelling study (33) also emphasizes cloud-environment feedbacks as an agent of microphysical invigoration. Like ours, this study finds that higher  $N_c$  increases humidity in RCE, and it shows that the humidity increase is driven by changes in cloud evaporation. Additionally, it shows that the increase in cloud evaporation invigorates convection without the need for ice-phase microphysics, although it focuses on changes in mass fluxes in RCE rather than changes in peak vertical velocities under WTG.

Because the humidity-entrainment mechanism is reliant on aerosol-induced changes in environmental relative humidity, it can only operate in environments where relative humidity is sensitive to changes in cloud detrainment. Under conditions with relatively weak mean vertical motion, relative humidity responds strongly to changes in detrainment and the humidity-entrainment mechanism operates effectively. Under conditions that promote large-scale ascent, on the other hand, the troposphere is driven toward saturation by the large-scale flow regardless of detrainment from clouds. As a result, relative humidity no longer responds strongly to changes in detrainment and aerosol changes no longer have a strong effect on peak updraft velocities.

In the tropics, the storms with the highest echo-top heights do not occur in regions of high mean precipitation with strong mean ascent; rather, they occur in convective margins (8). Similarly, peak tropical lightning flash rates occur in regions with a moderate lower-tropospheric saturation deficit rather than in regions where large-scale ascent pushes the atmosphere toward saturation (34). These regions—where the troposphere is moderately dry and convection is not strongly forced by mean ascent—are the same regions where the humidity-entrainment mechanism is likely to operate most effectively. In other words, our results suggest that aerosols may invigorate updrafts most effectively in regions of the tropics where extreme updraft speeds are already highest.

The simulations on which this work is based are all run into a steady state, and the humidity-entrainment invigoration mechanism occurs because of the steady-state response of tropospheric humidity to microphysical changes. The real tropical atmosphere, on the other hand, is dominated by a rich variety of weather systems, and whether this mechanism can operate effectively in the real world will depend in part on how rapidly tropospheric humidity can adjust to changes cloud microphysics. Some previous modeling work has suggested that moistening by cumulus congestus can substantially alter atmospheric over relatively short timescales of one to two days (35), in rough agreement with theoretical scalings based on radiative subsidence velocities (36, 37). In general, however,

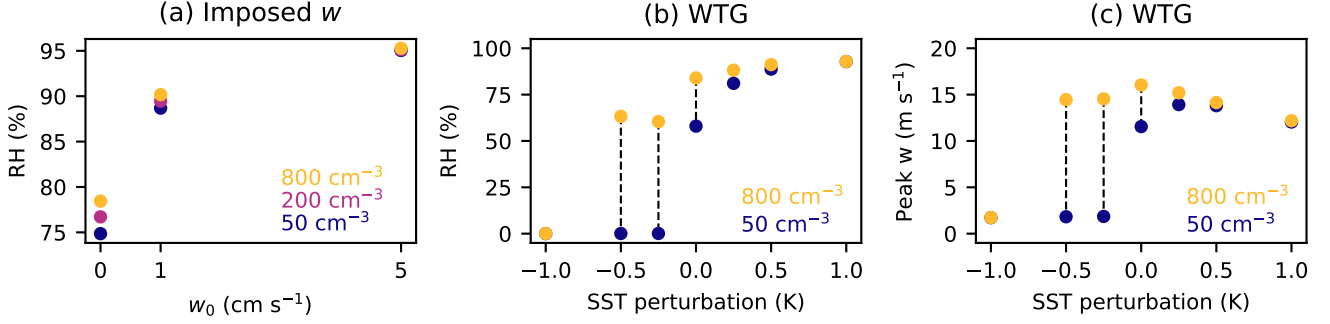


**Fig. 5.** (a) 2-6 km relative humidity in RCE simulations with imposed vertical motion, calculated using a linear combination of saturation vapor pressures over liquid and ice weighted by the fraction of cloud water mass in each phase and a mass-weighted vertical average. (b,c) 2-6 km relative humidity and peak vertical velocities from WTG-constrained simulations. Relative humidity is calculated as in panel (a), and peak vertical velocities are calculated as the maximum of the 99.99th percentile vertical velocity profile. Black dashed lines connect simulations that are identical except for the liquid cloud droplet number concentration.

timescales of humidity adjustment for a WTG-constrained atmosphere are poorly understood, and this work emphasizes its importance as a subject for future research.

Finally, because the humidity-entrainment mechanism relies on a three-way link between aerosol concentrations, tropospheric humidity, and convective vigor—all of which are either directly or indirectly observable—our results provide a target for future observational work. If the connections found in our idealized models are also detectable in observations, they would point to a key pathway by which aerosols (including those produced by human activity) modify atmospheric convection in the tropics.

## Materials and Methods

**Simulations.** Our simulations use version 6.11.3 of the System for Atmospheric Modeling (SAM, 38) integrated in a doubly-periodic non-rotating domain at a horizontal resolution of 1 km. The vertical grid contains 64 levels, with 12 levels in the lowest km, 500 m vertical spacing between 1 km and 20 km, and the model top at 27 km. Gravity waves are damped by a sponge layer in the top third of the domain.

The bottom boundary is a fixed-temperature ocean surface, set to 300 K except in WTG simulations with perturbed SST. Surface fluxes of latent and sensible heat are calculated using bulk aerodynamic formulae with exchange coefficient from Monin-Obukhov theory, and subgrid-scale fluxes in the atmosphere are parameterized using a first-order Smagorinsky scheme. Incoming solar radiation is set to an equinoctial diurnal cycle at 19.25 degrees from the equator, and radiative heating rates are calculated interactively using the Rapid Radiative Transfer Model (RRTM 39) with greenhouse gas concentrations are fixed at present-day levels. We initialize convection by adding a small amount of thermal noise near the surface, allow simulations to spin up for 40 days, and calculate statistics over the subsequent 20 days.

We run most of our simulations on a  $128 \times 128 \text{ km}^2$  domain. However, RCE mechanism denial experiments with the latent heat of fusion set to 0 self-aggregate in  $128 \times 128 \text{ km}^2$  domains. Because self-aggregation modifies environmental temperature profiles (e.g. 40), this complicates the comparison to RCE simulations with the default latent heat of fusion (which do not self-aggregate on  $128 \times 128 \text{ km}^2$  domains). Accordingly, the RCE simulations shown in Figures 2, 3, and 4 were run on a smaller  $64 \times 64 \text{ km}^2$  domain, which prevents the mechanism denial experiments from self-aggregating. The reduction in domain size has little effect on temperature, humidity, and vertical velocity profiles in RCE simulations with the default latent heat of fusion (compare Figures 2 and 3 with Figures S4 and S5). RCE simulations with imposed large-scale vertical motion, all WTG

simulations, and the RCE simulation used to generate the WTG reference temperature profile all use  $128 \times 128 \text{ km}^2$  domains.

**Parameterizations of large-scale dynamics.** The WTG-based parameterization of large-scale dynamics is based largely on the “conventional WTG” formulation in (41). During each time step, the parameterization first diagnoses a large-scale vertical velocity based on differences between horizontally-averaged temperatures and a reference profile and then calculates large-scale tendencies by vertically advecting horizontal-average profiles. The vertical velocity  $w_{WTG}$  is calculated as

$$w_{WTG}(z) = \frac{1}{\tau_{WTG}} \sin\left(\frac{\pi z}{h}\right) \left(\frac{\bar{s} - s_0}{\partial_z \bar{s}}\right) \quad [9]$$

Here,  $s = c_p T + gz$  is dry static energy, and  $g$  is the gravitational acceleration.  $s_0(z)$  is a reference dry static energy profile, which the parameterization takes as input,  $\bar{s}(z)$  is the horizontal-average dry static energy profile, and  $\partial_z \bar{s}$  is its vertical gradient (set to a minimum value of  $0.3 \text{ J kg}^{-1} \text{ m}^{-1}$ ). The WTG relaxation timescale  $\tau_{WTG}$  is calculated as the time required for a troposphere-deep gravity wave to propagate a distance  $L_{WTG}$ :

$$\tau_{WTG} = \frac{\pi L_{WTG}}{hN}. \quad [10]$$

$N^2$  is the Brunt-Vaisala frequency (a measure of stability to vertical displacements) calculated from horizontal-average profiles of potential temperature  $\bar{\theta}$  as

$$N^2 = \left\langle \frac{g}{\bar{\theta}} \frac{\partial \bar{\theta}}{\partial z} \right\rangle, \quad [11]$$

where angle brackets indicate a vertical average between  $z = 0$  and  $z = h$ . The factor of  $\sin(\pi z/h)$  is a mask that helps to produce vertical velocity profiles with structures similar to those found in the real tropical atmosphere, effectively making temperature relaxation timescales longer in the lower and upper troposphere, and the tropopause height  $h$  is defined as the height at which domain-average temperature profiles first drop below 210 K. We set  $L_{WTG}$  to 100 km, comparable to our simulation domains. Finally, we linearly taper  $w_{WTG}$  to 0 at the surface starting from a height of 1 km.

We use  $w_{WTG}$  to calculate source and sink terms for model fields by vertically advecting horizontal-average model fields. For a generic model field  $\phi$ , this gives a source term

$$\dot{\phi}_{WTG}(z) = -w_{WTG} \frac{\partial \bar{\phi}}{\partial z}. \quad [12]$$

We add source terms for liquid/ice water static energy (the prognostic thermodynamic variable used by SAM) and for all variables that represent mass concentrations of different water species (including water vapor, both phases of cloud water, and all classes of precipitating water).

The net effect of the WTG-based parameterization is to remove horizontal temperature differences relative to a reference state defined by  $s_0$  and, additionally, provide sources and sinks of moisture that are consistent with the removal of horizontal temperature gradients. In all WTG simulations, we use  $s_0(z) = c_p T_0(z) + gz$ , where  $T_0(z)$  is the time- and domain-average temperature profile from the last 20 days of an RCE simulation on a  $128 \times 128 \text{ km}^2$  domain with  $N_c = 50 \text{ cm}^{-3}$ .

We also use Equation 12 to calculate large-scale source terms for RCE simulations with imposed vertical motion, but with two differences from WTG simulations: the vertical velocity profile is prescribed rather than diagnosed interactively, and we include source terms for horizontal momenta and number concentrations of condensed water species as well as for liquid/ice water static energy and mass concentrations of water species.

**Scaling for impact of humidity on parcel temperatures.** We derived the scaling in Equation 3 from Equation 4 of (28), which uses a zero-buoyancy plume model to provide an expression for the difference between the temperatures of an entraining plume ( $T_{\text{entrain}}$ ) and an undilute moist adiabat ( $T_{\text{undilute}}$ ):

$$T_{\text{entrain}} - T_{\text{undilute}} = - \frac{L_v}{c_p + \frac{L_v^2 q^*}{R_v T^2}} \epsilon (1 - RH) \int_0^z q^*(z') dz', \quad [13]$$

where  $R_v$  is the specific gas constant for water vapor. If we now consider two entraining plumes that have identical properties at cloud base ( $z = 0$ ) but rise through environments with different relative humidities, we can write the temperature difference between the two plumes  $\Delta T_{\text{entrain}}$  as

$$\Delta T_{\text{entrain}} = \frac{L_v}{c_p + \frac{L_v^2 q^*}{R_v T^2}} \epsilon \Delta RH \int_0^z q^*(z') dz'. \quad [14]$$

The temperature difference is largest high in the atmosphere, where

$$\Delta T_{\text{entrain}} \approx \frac{L_v}{c_p} \epsilon \Delta RH \int_0^\infty q^*(z') dz'. \quad [15]$$

**Entraining plume model.** Following (28), this model assumes that the plume buoyancy is small, allowing us to write an equation for the evolution of plume moist static energy (MSE,  $h$ ) with height  $z$  as

$$\frac{dh}{dz} = -\epsilon L_v (q^* - q_v). \quad [16]$$

Here,  $\epsilon$  and  $q^*$  are the plume entrainment rate and the in-plume saturation specific humidity, and  $q_v$  is the specific humidity of the environment surrounding this plume. To solve this model, we integrate  $h$  upward from 500 m using the environmental temperature at 500 m from simulations as the initial condition. We diagnose  $q^*$  from  $h$  during the integration by assuming saturation in the plume and set  $q_v$  equal to domain- and time-mean water vapor profiles from simulations.

**ACKNOWLEDGMENTS.** We thank Xin Rong Chua, Yi Ming, and Raphael Rousseau-Rizzi for helpful discussions; and Marat Khairoutdinov for providing SAM. T.H.A. and T.W.C. were supported by NSF AGS 1740533: Convection and Rainfall Enhancement over Mountainous Tropical Islands.

1. Andreae MO, et al. (2004) Smoking Rain Clouds over the Amazon. *Science* 303:1337–1342.
2. Koren I, Kaufman YJ, Rosenfeld D, Remer LA, Rudich Y (2005) Aerosol invigoration and restructuring of Atlantic convective clouds. *Geophysical Research Letters* 32(14):1–4.
3. Lin JC, Matsui T, Pielke SA, Kummerow C (2006) Effects of biomass-burning-derived aerosols on precipitations and clouds in the Amazon Basin: A satellite-based empirical study. *Journal of Geophysical Research Atmospheres* 111(19).
4. Koren I, Remer LA, Altartaz O, Martins JV, Davidi A (2010) Aerosol-induced changes of convective cloud anvils produce strong climate warming. *Atmospheric Chemistry and Physics* 10(10):5001–5010.
5. Li Z, et al. (2011) Long-term impacts of aerosols on the vertical development of clouds and precipitation. *Nature Geoscience* 4(12):888–894.
6. Niu F, Li Z (2012) Systematic variations of cloud top temperature and precipitation rate with aerosols over the global tropics. *Atmospheric Chemistry and Physics* 12(18):8491–8498.
7. Williams E, Stanfill S (2002) The physical origin of the land-ocean contrast in lightning activity. *C. R. Physique* 3:1277–1292.

8. Zipser EJ, Cecil DJ, Liu C, Nesbitt SW, Yorty DP (2006) Where are the most intense thunderstorms on Earth? *Bulletin of the American Meteorological Society* August:1057–1071.
9. Cecil DJ, Buechler DE, Blakeslee RJ (2014) Gridded lightning climatology from TRMM-LIS and OTD: Dataset description. *Atmospheric Research* 135-136:404–414.
10. Thornton JA, Virts KS, Holzworth RH, Mitchell TP (2017) Lightning enhancement over major oceanic shipping lanes. *Geophysical Research Letters* 44(17):9102–9111.
11. Altartaz O, Koren I, Remer LA, Hirsch E (2014) Review: Cloud invigoration by aerosols—Coupling between microphysics and dynamics. *Atmospheric Research* 140-141:38–60.
12. Rosenfeld D, Sherwood S, Wood R, Donner L (2014) Climate Effects of Aerosol-Cloud Interactions. *Science* 343(6169):379–380.
13. Tao WK, Chen JP, Li Z, Wang C, Zhang C (2012) Impact of aerosols on convective clouds and precipitation. *Reviews of Geophysics* 50(2).
14. Fan J, Wang Y, Rosenfeld D, Liu X (2016) Review of aerosol-cloud interactions: Mechanisms, significance, and challenges.
15. Rosenfeld D, et al. (2008) Flood or Drought: How Do Aerosols Affect Precipitation? *Science* 321:1309–1313.
16. Fan J, et al. (2018) Substantial convection and precipitation enhancements by ultrafine aerosol particles. *Science* 359:411–418.
17. Roms DM (2014) An Analytical Model for Tropical Relative Humidity. *Journal of Climate* 27:7432–7449.
18. Singh MS, Warren RA, Jakob C (2019) A steady-state model for the relationship between humidity, instability, and precipitation in the tropics. *Journal of Advances in Modeling Earth Systems*.
19. Chua XR (2019) Ph.D. thesis (Princeton University).
20. Singh MS, O’Gorman PA (2015) Increases in moist-convective updraught velocities with warming in radiative-convective equilibrium. *Quarterly Journal of the Royal Meteorological Society* 141(692):2828–2838.
21. Morrison H, Curry JA, Khvorostyanov VI (2005) A New Double-Moment Microphysics Parameterization for Application in Cloud and Climate Models. Part I: Description. *Journal of the Atmospheric Sciences* 62:1665–1677.
22. Barahona D, Sotiropoulou R, Nenes A (2011) Global distribution of cloud droplet number concentration, autoconversion rate, and aerosol indirect effect under diabatic droplet activation. *Journal of Geophysical Research* 116.
23. Albrecht BA (1989) Aerosols, Cloud Microphysics, and Fractional Cloudiness. *Science* 245:1227–1230.
24. Sobel AH, Nilsson J, Polvani LM (2001) The Weak Temperature Gradient Approximation and Balanced Tropical Moisture Waves\*. *Journal of the Atmospheric Sciences* 58:3650–3665.
25. Morrison H, Grabowski WW (2013) Response of tropical deep convection to localized heating perturbations: Implications for aerosol-induced convective invigoration. *Journal of the Atmospheric Sciences* 70(11):3533–3555.
26. Blossley PN, Bretherton CS, Thornton JA, Virts KS (2018) Locally Enhanced Aerosols Over a Shipping Lane Produce Convective Invigoration but Weak Overall Indirect Effects in Cloud-Resolving Simulations. *Geophysical Research Letters* 45(17):9305–9313.
27. Seeley JT, Roms DM (2016) Tropical cloud buoyancy is the same in a world with or without ice. *Geophysical Research Letters* 43(7):3572–3579.
28. Singh MS, O’Gorman PA (2013) Influence of entrainment on the thermal stratification in simulations of radiative-convective equilibrium. *Geophysical Research Letters* 40(16):4398–4403.
29. Rosenfeld D, Lensky IM (1998) Satellite-Based Insights into Precipitation Formation Processes in Continental and Maritime Convective Clouds. *Bulletin of the American Meteorological Society* November:2457–2476.
30. Lutsko NJ, Cronin TW (2018) Increase in Precipitation Efficiency With Surface Warming in Radiative-Convective Equilibrium. *Journal of Advances in Modeling Earth Systems* 10(11):2992–3010.
31. Roms DM (2010) A direct measure of entrainment. *Journal of the Atmospheric Sciences* 67(6):1908–1927.
32. Anber UM, Wang S, Gentine P, Jensen MP (2019) Probing the Response of Tropical Deep Convection to Aerosol Perturbations Using Idealized Cloud-Resolving Simulations with Parameterized Large-Scale Dynamics. *Journal of the Atmospheric Sciences* 76(9):2885–2897.
33. Chua XR, Ming Y (2020) Convective invigoration traced to warm-rain microphysics.
34. Singh MS, Kuang Z, Maloney ED, Hannah WM, Wolding BO (2017) Increasing potential for intense tropical and subtropical thunderstorms under global warming. *Proceedings of the National Academy of Sciences of the United States of America* 114(44):11657–11662.
35. Hohenegger C, Stevens B (2013) Preconditioning deep convection with cumulus congestus. *Journal of the Atmospheric Sciences* 70(2):448–464.
36. Craig GC, MacK JM (2013) A coarsening model for self-organization of tropical convection. *Journal of Geophysical Research Atmospheres* 118(16):8761–8769.
37. Cronin TW, Wing AA (2017) Clouds, Circulation, and Climate Sensitivity in a Radiative-Convective Equilibrium Channel Model. *Journal of Advances in Modeling Earth Systems* 9(8):2883–2905.
38. Khairoutdinov MF, Randall Da (2003) Cloud Resolving Modeling of the ARM Summer 1997 IOP: Model Formulation, Results, Uncertainties, and Sensitivities. *Journal of the Atmospheric Sciences* 60(4):607–625.
39. Mlawer EJ, Taubman SJ, Brown PD, Iacono MJ, Clough SA (1997) Radiative transfer for inhomogeneous atmospheres: RRTM, a validated correlated-k model for the longwave. *Journal of Geophysical Research: Atmospheres* 102(D14):16663–16682.
40. Wing AA, Cronin TW (2016) Self-aggregation of convection in long channel geometry. *Quarterly Journal of the Royal Meteorological Society* 142(694):1–15.
41. Herman MJ, Raymond DJ (2014) WTG Cloud Modeling with Spectral Decomposition. *Journal of Advances in Modeling Earth Systems* 6(4).

# Supplementary Information for

## A humidity-entrainment mechanism for microphysical invigoration of convection

Tristan H. Abbott and Timothy W. Cronin

Tristan H. Abbott  
E-mail: [thabbott@mit.edu](mailto:thabbott@mit.edu)

### This PDF file includes:

Supplementary text  
Figs. S1 to S5  
SI References

arXiv:2002.06056v1 [physics.ao-ph] 14 Feb 2020

## Supporting Information Text

### 1. Plume calculations for weakly-forced WTG simulations

The plume calculation that reproduces high-percentile temperatures from WTG-constrained simulations given environmental humidity profiles is similar to the plume model used to reproduce RCE temperature profiles. The main differences are (1) we include the effects of plume-environment temperature differences in the plume equation because differences between high-percentile and environmental temperatures increase with increasing  $N_c$  and (2) we assume that peak temperatures occur in updrafts with anomalously weak entrainment and use  $\epsilon = 0.15 \text{ km}^{-1}$  rather than  $1 \text{ km}^{-1}$ . The plume equation, solved as in the main text, is

$$\frac{dh}{dz} = -\epsilon[c_p(T - T_e) + L_v(q^* - q_v)], \quad [1]$$

where  $T$  is the plume temperature,  $T_e$  and  $q_v$  are the environmental temperature and specific humidity profiles taken from WTG simulations, and all other symbols denote the same quantities as in the main text.

High-percentile temperatures are warmer in high- $N_c$  WTG simulations (Figure S1a), but the temperature differences between simulations with different  $N_c$  are smaller than in RCE simulations even though moisture convergence caused by ascent in high- $N_c$  simulations produces specific humidity changes larger than those seen in RCE simulations (Figure S1b). This is largely because the mixing of dry static energy between the plume and the environment relaxes plume temperatures toward environmental temperatures, which are nearly  $N_c$ -independent owing to WTG constraints. This relaxation cools high- $N_c$  plumes more than low- $N_c$  plumes, limiting the temperature difference. With the plume-environment temperature difference included, the plume model approximately reproduces peak temperature differences from WTG simulation (Figure S1c).

### 2. Sensitivity of relative humidity to detrainment changes

Differentiating Equation 8 from the main text and multiplying by  $\delta_T$  gives an expression for the sensitivity of relative humidity to fractional changes in the detrainment rate:

$$\frac{\partial RH}{\partial \ln \delta_T} = \frac{\delta_t \frac{M_d}{M_u} \gamma}{\left(\delta_T + \frac{M_d}{M_u} \gamma\right)^2}. \quad [2]$$

In turn, this can be re-written in terms of the RCE relative humidity

$$RH^* = \frac{\delta_T}{\delta_T + \gamma} \quad [3]$$

as

$$\frac{\partial RH}{\partial \ln \delta_T} = \frac{\frac{M_d}{M_u} \frac{RH^*}{1 - RH^*}}{\left(\frac{M_d}{M_u} + \frac{RH^*}{1 - RH^*}\right)^2} \quad [4]$$

The sensitivity is largest when  $M_d/M_u = RH^*/(1 - RH^*)$ . Near RCE, where large-scale vertical motion is weak and  $M_d/M_u \approx 1$ , tropospheric relative humidity is typically 0.6 to 0.8 (e.g., 1). This corresponds to  $RH^*/(1 - RH^*) \approx 1.5$  to 4, which is larger than  $M_d/M_u$ . As a result, the sensitivity of relative humidity to detrainment should be smaller in the presence of large-scale ascent ( $M_d/M_u < 1$ ) than in RCE ( $M_d/M_u = 1$ ). The sensitivity only increases moving away from RCE into a regime with mean ascent if  $RH^* < 0.5$ , much smaller than is typical in RCE (Figure S2).

### 3. SST perturbation experiments

Our WTG simulations appear to be only marginally stable to the development of large-scale circulations (consistent with bistability found in previous modeling studies (2, 3)) and can easily be pushed into moist regimes with strong ascent or dry regimes with strong subsidence and no deep convection by small changes in SST (Figure S3). The transition to a moist regime as SST increases seems to result from a jump between distinct equilibria rather than a gradual shift of a single equilibrium: a small increase in SST pushes the simulations into a limit cycle where domain-average precipitation rates vary between about 5 and 30  $\text{mm day}^{-1}$ , and larger SST increases allow the simulations to remain in the high-precipitation state. Similarly, simulations with decreased SST either remain in a state with precipitation rates near that of the RCE simulations or jump to a dry state with no precipitation.

Although these regime transitions make it difficult to produce gradual changes in large-scale vertical motion by gradually changing SST, we can nevertheless contrast the impact of aerosol perturbations in three regimes: one RCE-like with weak vertical motion (including most simulations with SST perturbations less than about 0.25 K in magnitude), one with strong upward motion (simulations with SST perturbations of  $\sim 0.5$  K and above), and one with strong subsidence (SST perturbations of  $\sim -0.5$  K and below).

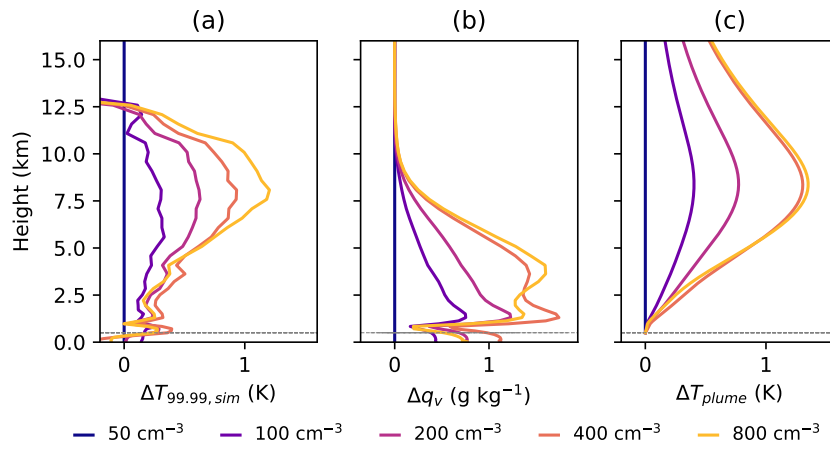


**Fig. S1.** Differences from an  $N_c = 50 \text{ cm}^{-3}$  control of (a) 99.99th percentile temperature profiles and (b) mean specific humidity profiles from WTG simulations, and (c) temperature profiles from the plume model described in Supporting Text 1. The dashed grey line shows the level where the plume model calculation is initiated.

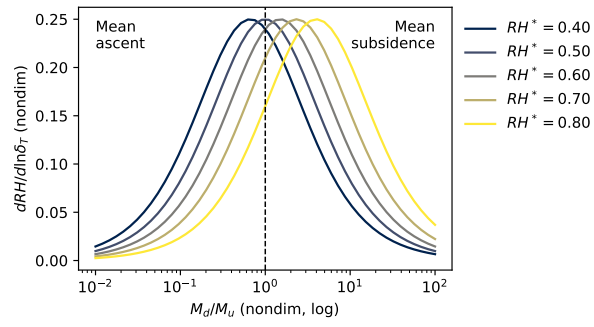


**Fig. S2.** Sensitivity of relative humidity to changes in the effective detrainment rate (Equation 2) for different values of RCE relative humidity  $RH^*$ . The black dashed line indicates  $M_d/M_u = 1$  (i.e., RCE), and upward motion increases moving to the left.

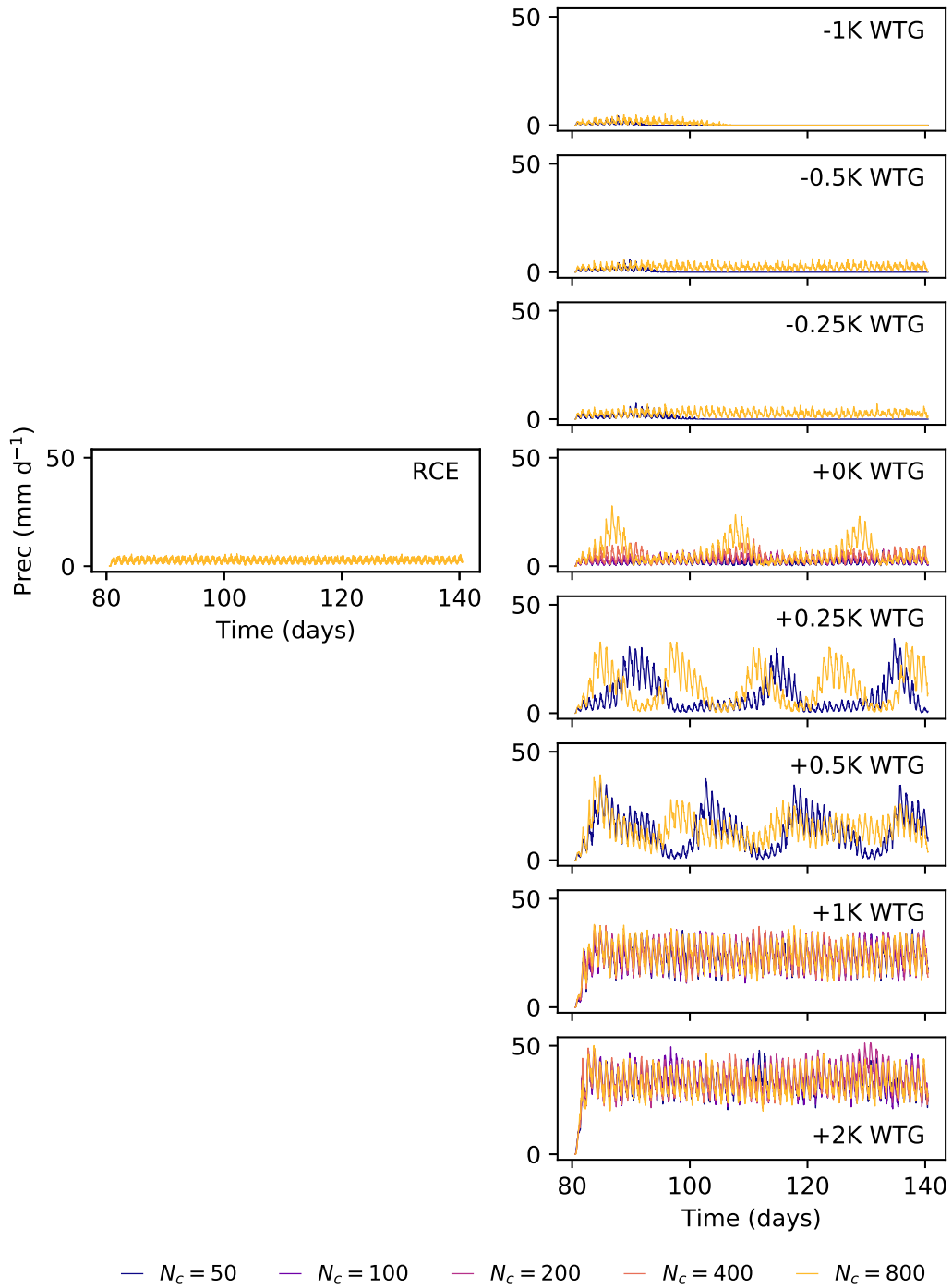


**Fig. S3.** Domain-average precipitation timeseries in (top row) WTG simulations with SST increases and (bottom row) RCE simulations and WTG simulations with SST decreases. The vertical axis is the same within each row but differs between rows. All panels include simulations with  $N_c = 50 \text{ cm}^{-3}$  and  $N_c = 800 \text{ cm}^{-3}$ , but not all include intermediate  $N_c$ .

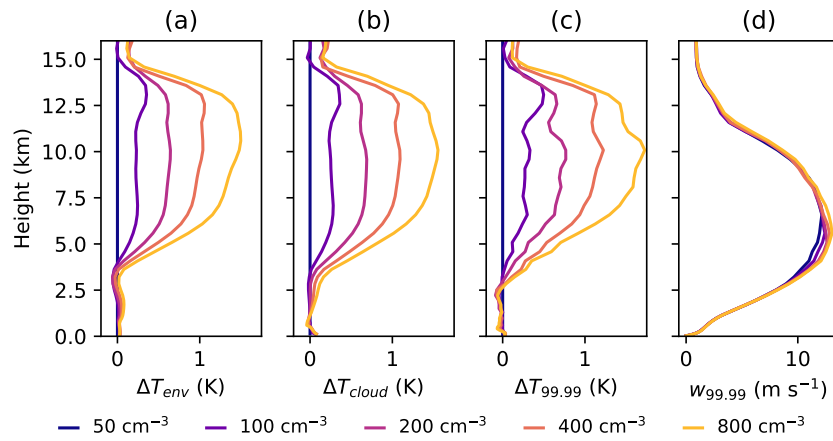


**Fig. S4.** As in Figure 2 in the main text, but for RCE simulations on a  $128 \times 128 \text{ km}^2$  domain. Panels (a-c) show differences from a control RCE simulation (with  $N_c = 50 \text{ cm}^{-3}$ ) in (a) domain- and time-mean temperatures ( $T_{env}$ ), (b) mean temperatures in cloudy updrafts ( $T_{cloud}$ ), and (c) 99.99th percentile temperatures at each level ( $T_{99.99}$ ). Panel (d) shows 99.99th percentile vertical velocities at each level.

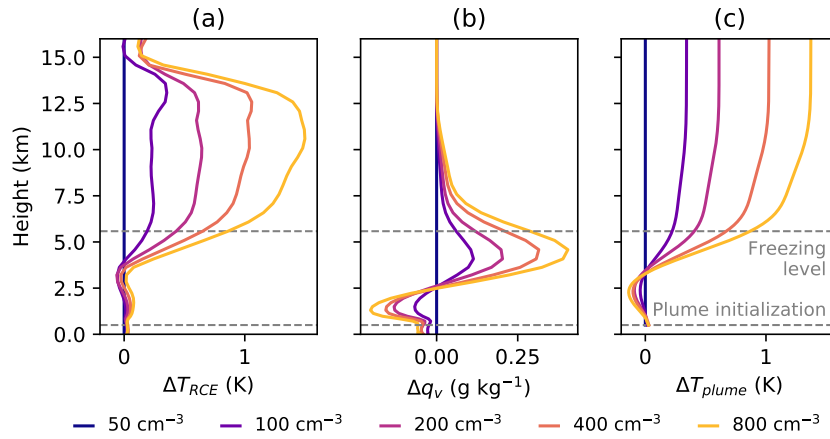


**Fig. S5.** As in Figure 3 in the main text, but for RCE simulations in a  $128 \times 128 \text{ km}^2$  domain and without profiles from simulations with the latent heat of fusion set to 0. Panels (a-b) show differences from a control RCE simulation (with  $N_c = 50 \text{ cm}^{-3}$ ) in (a) domain- and time-mean temperature profiles and (b) domain- and time-mean specific humidity profiles from RCE simulations used as input for plume calculations. Panel (c) shows environmental temperature profiles from plume calculations (details in text). The gray dashed line at 500 m shows the level where plume calculations are initialized with domain- and time-mean temperatures from simulations, and the gray dashed line near 5 km indicates the level where clouds begin to freeze, calculated as the lowest model level where more than 5% of the mean cloud water mass is ice. (Only one line is shown because this definition of the freezing level is identical in all simulations.)

## References

1. Roms DM (2014) An Analytical Model for Tropical Relative Humidity. *Journal of Climate* 27:7432–7449.
2. Sobel AH, Bellon G, Bacmeister J (2007) Multiple equilibria in a single-column model of the tropical atmosphere. *Geophysical Research Letters* 34(22).
3. Sessions SL, Sugaya S, Raymond DJ, Sobel AH (2010) Multiple equilibria in a cloud-resolving model using the weak temperature gradient approximation. *Journal of Geophysical Research Atmospheres* 115(12).